The unique features in the four-day widespread extreme rainfall event over North China in July 2023

Jinfang Yin[1, 2, 3], Feng Li[1], Mingxin Li[1], Rudi Xia[1], Xinghua Bao[1],
Jisong Sun[1], and Xudong Liang[1]

[1] State Key Laboratory of Disaster Weather Science and Technology, Chinese Academy of Meteorological Sciences, Beijing 100081, China
[2] Research Center for Disastrous Weather over Hengduan Mountains & Low-Latitude Plateau, China Meteorological Administration (CMA), Kunming 650034, China
[3] Shigatse National Climatological Observatory, CMA, Shigatse 857000, China

Submitted to *Natural Hazards and Earth System Sciences* (*NHESS*)
August 2024
Second round November 2024

Corresponding author: Jinfang YIN
E-mail: yinjf@cma.gov.cn

ABSTRACT

Synoptic forcings have traditionally played a pivotal role in extreme rainfall over North China. However, there are still large unexplained gaps in understanding the formation of extreme rainfall events over this region. The heavy rainfall event, lasting from 29 July to 2 August 2023 (referred to as "23·7" event), is characterized by long duration, widespread coverage, and high accumulated rainfall over North China. Overall, the persistent extreme rainfall is closely associated with the remnant vortex originating from typhoon Doksuri (2305), tropical storm Khanun (2306), and the unusual westward extended Western North Pacific Subtropical High (WNPSH), as well as quasi-stationary cold dry air masses surrounding North China on the west and north sides. Based on wind profiles and rainfall characteristics, the life cycle of the "23·7" event is divided into two stages. In the first stage, the western part of the WNPSH was weakened by tropical storm Doksuri, appearing that the WNPSH retreated eastward with decreasing height. The marginal zone of this subtropical high became then inclined below 500 hPa. Therefore, convection was limited by the tilted WNPSH with a warm-dry cover embedded in the low-to-middle troposphere. Meanwhile, mountain land in the western part of North China was occupied by cold air masses above nearly 3.0 km. Combining the orographic and cold air blockings, only a thin layer of southeasterly wind (between 1.3 and 3.0 km) can overpass mountains. Although the warm and moist southeasterly flows were lifted by orography, no convections were triggered because of the local capped cold and dry air masses overhead. Under this regime, equivalent potential temperature (θ_e) gradients were established between warm humid and dry cold air masses, similar to a warm front, causing warm air to lift and generate widespread rainfall but low intensity. However, the lifting was too weak to allow convection to be highly organized. In the second stage, the WNPSH was further weakened by enhanced Khanun, and thus the embedded warm-dry cover associated with the tilted WNPSH was significantly thinned. Consequently, convection triggered by orographic blocking is able to extend upward and consequently further develop, forming deep convections. Generally speaking, the convections in the second stage are much deeper than those in the first stage. The results may shed new light on better understanding and forecasting of long-lasting extreme rainfall.

1. Introduction

A persistent severe rainfall event occurred over central and North China during the period from 29 July to 2 August 2023 (referred to as "23·7" event), which was regarded as one of the precipitation extremes of 2023 globally (Fowler et al., 2024). Despite the rainfall in low intensity, it was long-lasting and widespread, resulting in large accumulated rainfall. Overall, the average accumulated rainfall over North China (including Beijing, Tianjin, and Hebei Province) was 175 mm, which was approximately 1/3 of the average annual precipitation in this region. Flooding from this event affected 1.3 million people, bringing severe human casualties and economic losses. The sustained severe rainfall over Beijing left 33 people dead and 18 missing persons. One of the distinct features of this rainfall event was closely associated with the remnant vortex originating from typhoon Doksuri (2305), tropical storm Khanun (2306), unusual westward extended Western North Pacific Subtropical High (WNPSH), and quasi-stationary cold dry air masses surrounding North China on their west and north sides.

It is common for rainfall occurrence over North China due to strong water vapor supply by tropical cyclones over the East China Sea and/or Southern China Sea (e.g., Ding,1978; Feng and Cheng,2002; Yin et al.,2022c). Like the "96·8" severe rainfall event (Sun et al.,2006; Bao et al., 2024), the present persistent rainfall event was closely linked to two tropical storms of Doksuri (2305) and Khanun (2306). Note that the Doksuri weakened to a typhoon remnant vortex (typhoon-low pressure) at this moment as it moved inland after landfalling, while the tropical storm Khanun was in a fast-developing stage. The tropical storm Khanun and the typhoon remnant vortex built jointly a water vapor bridge, transporting a large amount of water vapor to North China from the East China Sea. Previous studies (e.g., Hirata and Kawamura, 2014; Gao et al.,2022; Yang et al.,2017) pointed out that large amounts of water vapor brought by a typhoon over the North Pacific were favorable for severe rainfall generation in eastern China.

In the last several decades, considerable attention was paid to the remote rainfall events associated with tropical cyclones, with substantial progress made (e.g., Wang et al.,2009; Xu et al.,2023a; Xu et al.,2023b; Lin and Wu,2021). Commonly, sufficient water vapor provided by a tropical cyclone plays an important role in extreme rainfall over North China (e.g., Rao et al.,

2023; Xu et al.,2023b). Besides, many studies confirmed that the WNPSH is closely related to water vapor transportation and the spatial distribution of rainfall (e.g., Hu et al.,2019; Gao et al., 2022). Additionally, orographic forcing of the approaching warm and moist unstable airflow plays a critical role in determining the location of convection initialization, although sometimes orographic forcing played a small role compared to Typhoon's circulation (Wang et al.,2009). Moreover, severe rainfall can be generated by the complicated cloud microphysical processes due to the interactions between tropical oceanic warm-moist and mid-latitude cold-dry air masses (Wang et al.,2009; Xu and Li,2017; Xu et al.,2021). Despite some experiences gained, there are still large unexplained gaps in understanding the formation of extreme rainfall (Meng et al.,2019).

Due to the tremendous impacts of the "23·7" event, many scholars have carried out studies of the event from various aspects. Li et al (2024) provided a detailed analysis of fine characteristics of the precipitation using radar and dense rain gauge observations. Xia et al. (2025) investigated extreme hourly rainfalls at different episodes. Fu et al. (2023) paid attention to the effects of dynamic and thermodynamic conditions on precipitation, while Gao et al. (2024) focused on the impact of mountain-plain thermal contrast on precipitation distribution. Although operational forecasts gave a reasonable spatial distribution of precipitation at that time, the precipitation intensity was underestimated significantly. Indeed, it is found that, in this event, the unusual westward-extended WNPSH played an important role in modulating convection initialization and development with several unusual features revealed. However, given the unusual westward-extended WNPSH, some unexplainable questions have been raised, while little attention has been paid to date. Firstly, what mechanism(s) could account for the persistent severe rainfall? Besides, what is the role of the unusual westward-extended WNPSH in governing the rainfall over North China? Therefore, we are motivated to conduct the present modeling study to answer those questions.

The rest of the paper is organized as follows. A detailed description of the main features of extreme rainfall and synoptic-scale weather conditions is documented. Section 3 provides detailed model configuration and verification against observations. We present a detailed analysis of the extreme rainfall production in Section 4. The paper finishes with conclusions

and outlooks.

2. Properties of rainfall and wind profiles

2.1 Characteristics of rainfall

Figure 1 shows the spatial distribution of 96-h accumulated rainfall from observations during the period from 0000 UTC 29 July to 0000 UTC 2 August 2023, with the peak amount of 1004 mm at Liangjiazhuang station near Xingtai, Hebei Province of North China. Exceptionally long duration of rainfall is a notable feature of the event, with the longest duration being 80 hours within the four days at some stations. The spatial distribution of the rain belt with three severe rainfall cores is consistent with the orography direction of the Yanshan Mountains on the north as well as of the Taihang Mountains on the south, suggesting that orography plays an important role in the precipitation. It should be emphasized that three rainfall cores, marked by Mentougou (MTG, 741 mm) in Beijing, and Yixian (YX, 753 mm) and Xingtai (XT, 1004 mm) in Hebei Province, correspond respectively to the regions with large topographic gradients (Fig. 1). Please refer to Li et al. (2024) for a detailed analysis of fine features of this rainfall event.

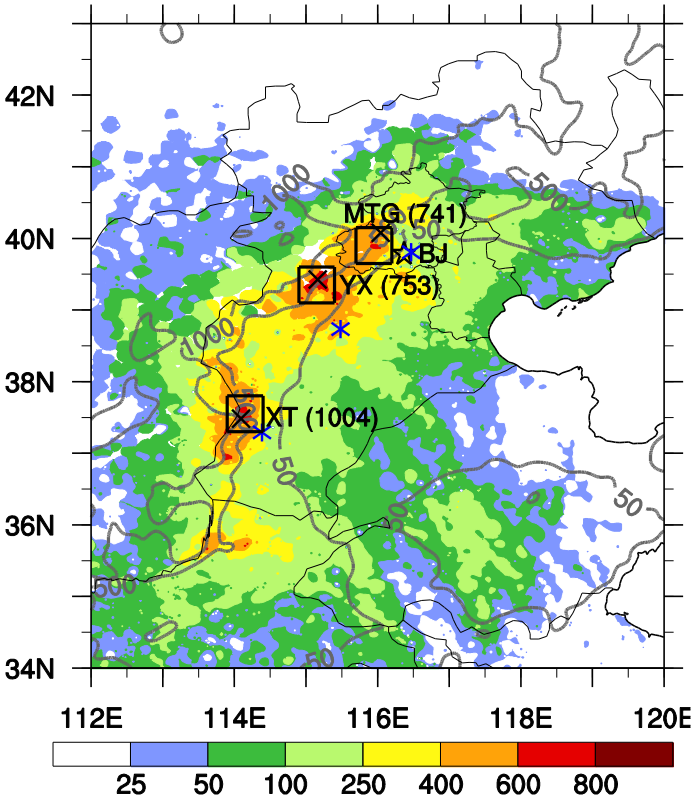

Fig. 1 Spatial distribution of 96-h accumulated rainfall (mm, shadings) from the intensive surface rain gauge observations during the period from 0000 UTC 29 July to 0000 UTC 2

August 2023; Gray contours denote orography from 50 m to 1000 m as marked. Three rainfall cores in Mentougou (MTG) in Beijing, and Yixian (YX) and Xingtai (XT) in Hebei Province are denoted by squares, with the values in parentheses indicating the maximum accumulated rainfall (marked by crisscross sign ×) for the regions, respectively. The blue asterisks (∗) represent the locations of wind profiler observational stations near the three rainfall cores. The start (☆) sign indicates the location of Beijing (BJ) City. (Similarly for the rest of figures).

2.2 Wind profiles

The observed wind profiles near MTG, YX, and XT are shown in Fig. 2. It is found that temporal variations in horizontal wind fields are distinct during the rainfall event. Taking the wind profiles near MTG as an example (Fig. 2a), the easterly or southeasterly wind at the levels below 4 km was increased gradually from 2 m s^{-1} at 1200 UTC 28 to 24 m s^{-1} at 1200 UTC 30 July 2023. The easterly or southeasterly wind lasted to 0400 UTC 31 July 2023, turned southerly except for near the ground, and then turned southwesterly near 0400 UTC 1 August 2023. After 0400 UTC 31 July, wind speed decreased significantly and then increased drastically. More specifically, the wind speed was decreased from 8 m s^{-1} to 2 m s^{-1}, and then increased to 14 m s^{-1} near 1 km above the ground. However, opposite variations were observed above 4 km. One can see that the horizontal wind shifted from southwesterly to southerly, then back to southwesterly. Overall, the shift in wind direction and speed altered the vertical wind shear, which directly affected the development and organization of subsequent convection (Pucik et al., 2021). Similar variations can also be found at YX and XT stations, although the timing of changes is not synchronized with each other (Fig. 2c, d). The variations proceeded from south to north, starting first at XT and finally at MTG, in pace with the typhoon moving from south to north.

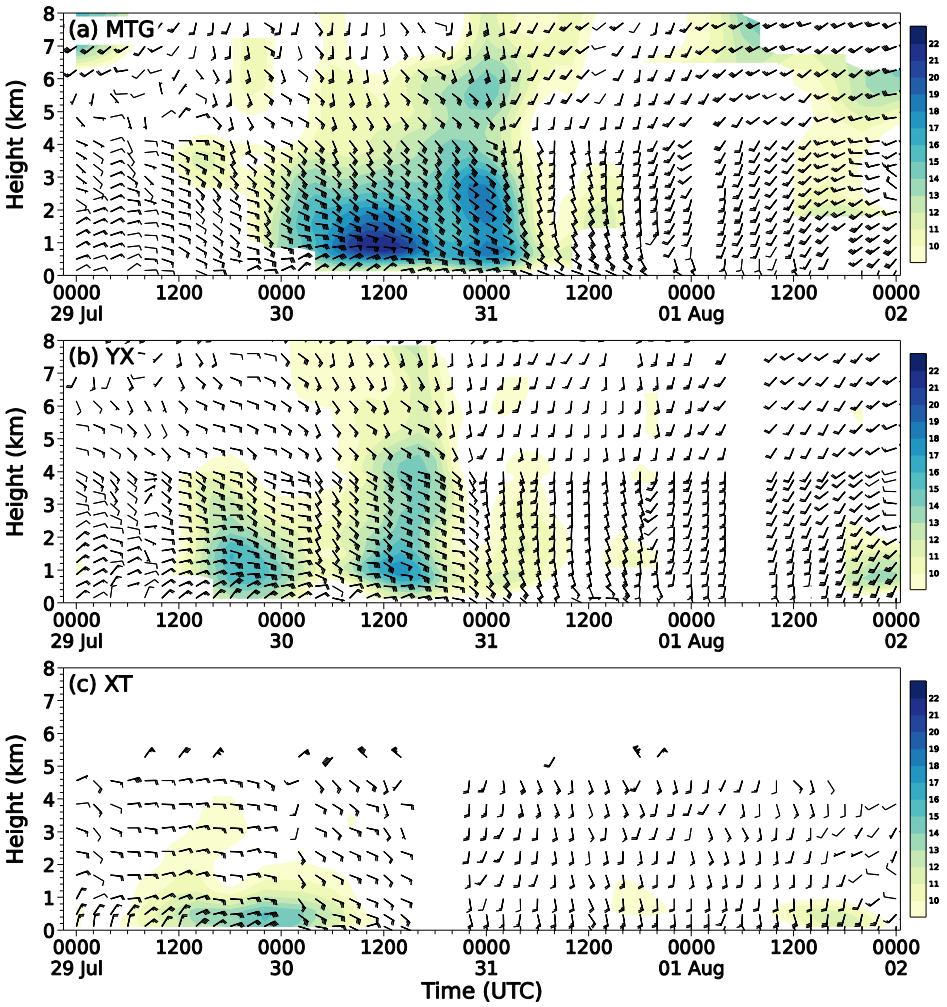

147

148 **Fig. 2** Temporal evolution of the wind profile (a full barb is 4 m s^{-1}, and shadings denote wind
149 speed over 10 m s^{-1}) from observations near (a) MTG, (b) YX, and (c) XT during the period of
150 0000 UTC 29 July to 0000 UTC 2 August 2023. Note that only the wind profile below 5 km
151 above the ground is able to be observed due to the limitation of the instrumentation near
152 Xingtai (XT). (see Fig. 1 their locations).

153 ***2.3 Synoptic conditions on 28 July 2023***

154 Figure 3 displays a weather chart on 500 hPa at 1200 UTC 28 July 2023. One can see that
155 the large-scale flow patterns exhibited a coexistence of the tropical storm Khanun (2306) with a
156 remnant vortex originating from typhoon Doksuri (2305)*. Note that the Khanun was in the
157 rapid development stage then, while the vortex weakened significantly at that time. Another
158 important weather system was the WNPSH (denoted by the 588 isoline) with a square-head

*The typhoon Doksur i(2305) weakened to a typhoon remnant vortex as it was passing through East China's Anhui Province. The China Meteorological Administration (CMA) stopped issuing updates on the Doksuri at 0300 UTC 29 July 2023. The remnant of Doksuri remained in a vortex in the lower troposphere, although its wind force diminished as it moved northward.

shape on its western border. Clearly, a water vapor transportation passage was built due to the cyclonic circulation of the tropical storm in combination with the anticyclonic circulation on the southwestern part of the WNPSH. As a result, central and North China was covered by high precipitable water (PW) of over 68 mm. Similar patterns can be viewed at the level of 850 hPa (not shown).

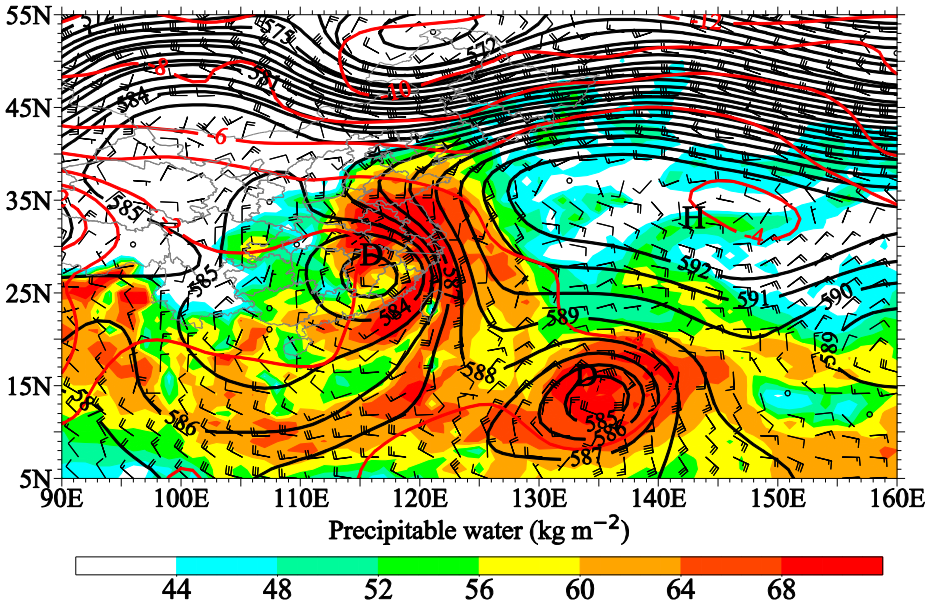

Fig. 3 Weather chart on 500 hPa at 1200 UTC 28 July 2023: Geopotential height (black-contoured at 15 gpm intervals), temperature (red-contoured at 2°C intervals), wind barbs (a full barb is 4 m s^{-1}), and precipitable water (kg m^{-2}, shadings).

3. Model configuration and verification

3.1 Model description

In this study, the persistent severe rainfall event is reproduced with the WRF model version 4.1.3. The WRF model is configured in two-way nested grids of horizontal grid sizes of 9 km, 3 km, and 1 km. Figure 4 displays the geographical coverage of the WRF model domains, with the grid points of 901(nx)×601(ny), 973×1231, and 1231×1591 for the outer, intermediate, and inner domains, respectively. The outermost domain (i.e., D01) is centered at 115°E, 35°N, and a total sum of 58 sigma levels is assigned in the vertical with the model top fixed at 20 hPa. Since the rainfall is closely associated with the spatial distribution of orography over North China (Fig. 1), the Shuttle Radar Topography Mission (SRTM) high-resolution (90 m) topographic data is employed in the present simulation. It should be noticed that the model vertical level distribution was carefully tested and has achieved good performance (Yin et al., 2020; Yin et al.,2022a; Yin et al.,2018; Yin et al.,2022b). The WRF model physics schemes are configured with the YSU scheme for the planetary boundary layer (Hong et al., 2006), and the

revised MM5 Monin-Obukhov (Jimenez) scheme for the surface layer (Jiménez et al., 2012), as well as the Unified Noah Land Surface Model (Tewari et al.,2004). The rapid radiative transfer model (RRTM) (Mlawer et al.,1997) and the Dudhia scheme (Dudhia,1989) are used for longwave and shortwave radiative flux calculations, respectively. The Kain-Fritsch cumulus parameterization scheme (Kain,2004) is utilized for the outer two coarse-resolution domains but is bypassed in the finest domain (i.e., D03). The Thompson-ensemble cloud microphysics scheme is applied to the explicit cloud processes (Thompson et al.,2008; Yin et al.,2022a).

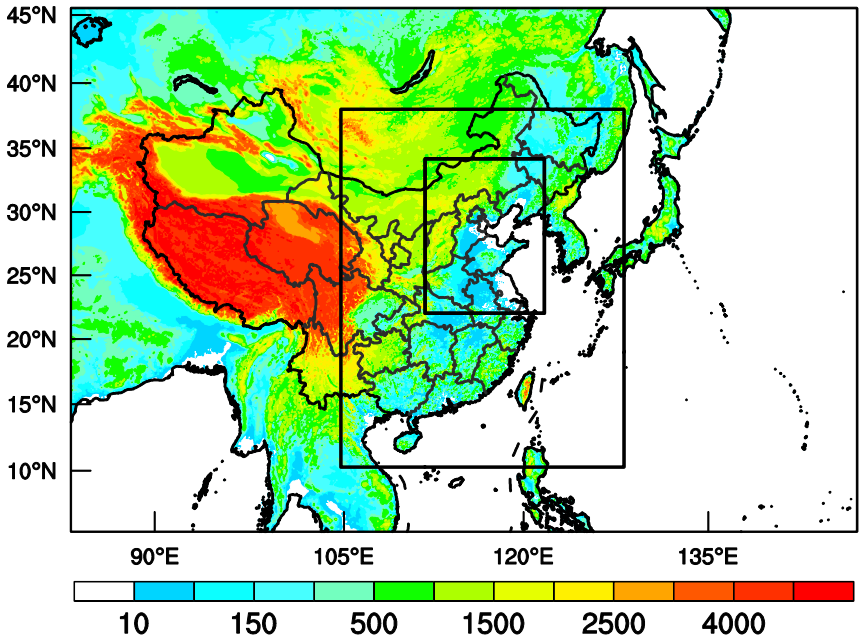

Fig. 4 The WRF model orography (m, shadings) and the nested model domains used for simulations with the grid sizes of 9 km (D01), 3 km (D02), and 1 km (D03).

The WRF model is integrated for 108 hours, starting from 1200 UTC 28 July 2023, with outputs at 6-min intervals. The model outputs in the first 12 h are considered as the spin-up process and thus are not used for the present work. The initial and outermost boundary conditions are interpolated from the final operational global analysis of 1-degree by 1-degree data at 6-h intervals from the Global Forecasting System of the National Centers for Environment Prediction (NCEP). In order to force large-scale fields consistent with the driving fields, grid analysis nudging is activated by performing the Four-Dimension Data Assimilation (FDDA) throughout the model integration (Bowden et al.,2012; Stauffer et al.,1991). The innermost domain (i.e., D03) outputs are validated and used for further analysis, and the outermost domain (i.e., D01) outputs are used to demonstrate weather-scale dynamical and thermal features. The wind profiler and surface hourly observations are provided by the National Meteorological Information Center (NMIC) of the China Meteorological

Administration (CMA) after strict quality control.

3.2 Model verification

Figure 5 shows the spatial distribution of 96-h accumulated rainfall from the simulation during the period from 0000 UTC 29 July to 0000 UTC 02 August 2023. Generally speaking, the WRF model replicates well the spatial distribution of severe rainfall. The rainfall belt with three rainfall cores coinciding with the orography is reproduced well, and the simulated extreme rainfall amount matches well with the observed. Note that the model produces a peak 96-h accumulated rainfall of 778 mm over the XT region, while the maximum rainfall of 1004 mm was observed over the XT region. Despite the simulation underestimates rainfall over this region, it captures the main features of rainfall over central and North China.

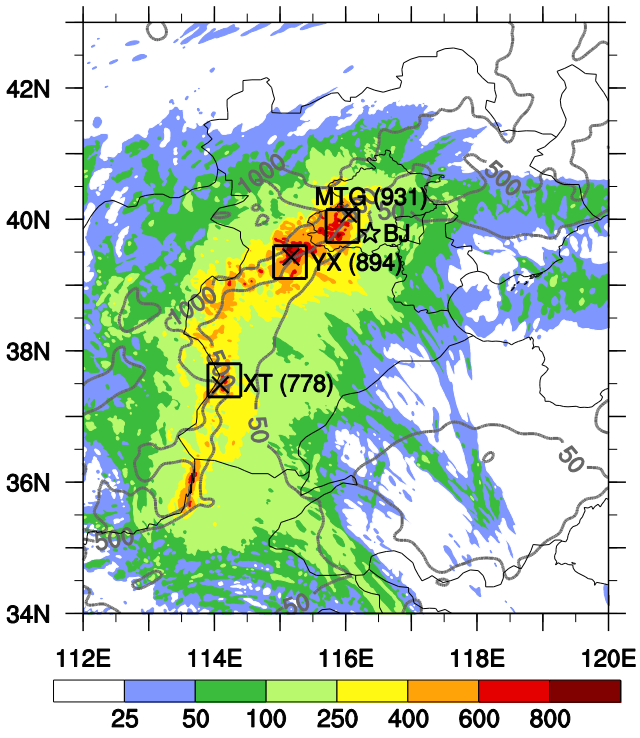

Fig. 5 Same as in Fig. 1 but for the simulated rainfall (mm, shadings).

Figure 6 compares the spatial distribution of daily rainfalls between observations and simulations during the period from 0000 UTC 30 July to 0000 UTC 2 August 2023. From observations, one can see that the daily rainfalls show obvious variations. On the first day (Fig. 6a), the rainfall occurred mainly in northern Henan Province and southern Hebei Province, on the east side of the Taihang Mountains with the rainfall cores over 250 mm. On the next day (Fig. 6b), the rainfall extended significantly northeastward, and a new strong rainfall core occurred, covering central Hebei Province and southwest Beijing. On the third day (Fig. 6c),

223 rainfall was significantly reduced in both coverage and intensity, mainly occurring in Beijing
224 and the surrounding areas. On the fourth day (Fig. 6d), rainfall moved eastward and weakened
225 rapidly. It is apparent that the model reproduces well the evolutions of the rainfall (Fig. 6e-h),
226 with general characteristics similar to the observed (Fig. 6a-d).

227 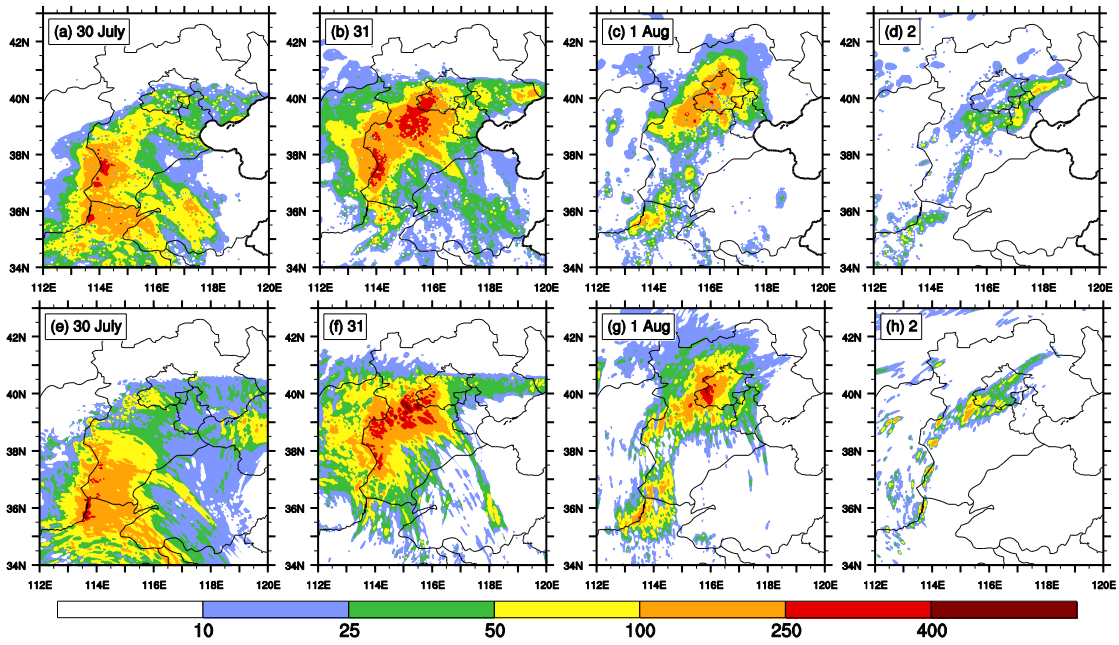

228

229 **Fig. 6** Spatial distribution of (a-d) observed and (e-h) simulated daily rainfall (mm) during the
230 period from 0000 UTC 30 July to 0000 UTC 2 August 2023.

231 Figure 7 compares the time series of hourly rainfall rates between the observed and the
232 simulated over the MTG, YX, and XT regions. The rainfall event is characterized by long
233 duration, widespread coverage, and high intensity. As has been mentioned above, the rainfall
234 extended from the south to the north, covering Henan Province, Hebei Province, and Beijing.
235 The rainfall first occurred in the XT region and ended near 0000 UTC 31 July 2023. In the wake
236 of that the rainfall belt moved northeastward, over both the MTG and YX regions rainfall
237 occurred, and it ended nearly at 0000 UTC 2 August. The observed timings of initiating and
238 ending of the rainfall event are well replicated by the WRF model, with the observed peaks
239 reproduced as well, although there are some timing biases. For example, the strongest rainfall
240 occurred over the MTG region during the period from 0000 UTC to 0600 UTC 31 July.
241 However, the simulated strongest rainfall has a 6-h lag, occurring from nearly 0600 UTC to
242 1200 UTC 31 July depending on the region. Overall, good agreements between the simulation
243 and observations are obtained in terms of the timing and location in the spatial distribution of

rainfall.

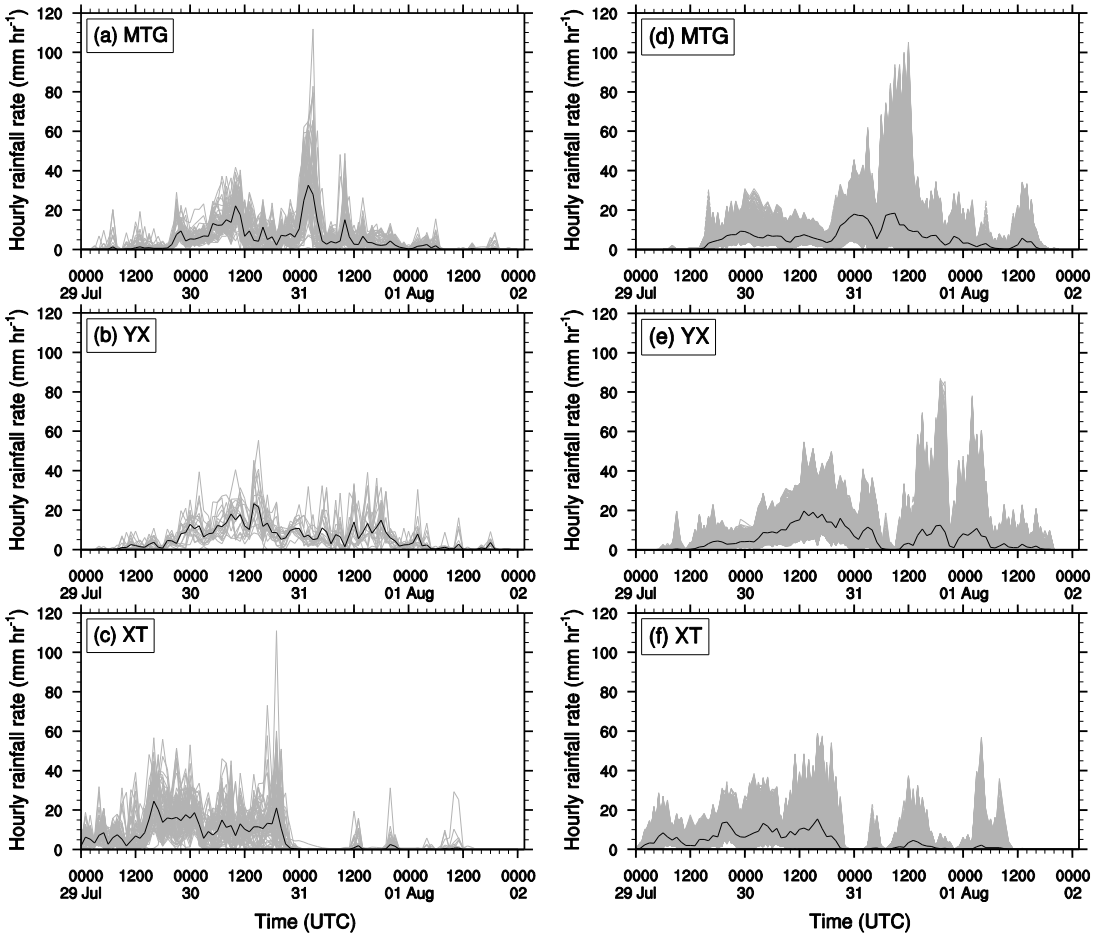

Fig. 7 Time series of (a-c) the rain gauge observations and (d-f) the simulated hourly rainfall rates (gray lines, mm hr^{-1}) for all the stations/grid points over the (a, d) MTG, (b,e) YX, and (c,f) XT regions during the period of 0000 UTC 29 July to 0000 UTC 02 August 2023. The black line denotes the domain-averaged hourly rainfall rates over all the stations (grid points) from observations (simulations). (see Fig. 1 for their locations). In total, 74, 19, and 67 observations are used for (a) MTG, (b) YX, and (c) XT, respectively. For the simulation, there are (d) 2296, (e) 2365, and (f) 2420 grid points, respectively.

The evolution of the simulated wind profile is presented in Fig. 8. Similar to the observed (Fig. 2), the simulated easterly wind increased gradually from nearly 1200 UTC 29 July, corresponding to the start of the precipitation (Fig. 6e-h). The horizontal wind shifted from easterly to southerly except for near the ground and then turned to southwesterly with wind speed decreasing significantly. Overall, the variations of the simulated wind profile were consistent with those observed, indicating that the WRF model was able to well capture the main features of the wind profile. Based on the wind profile and rainfall features, the simulated

rainfall process is roughly divided into two stages. The shift moments (roughly marked by thick black lines) are near at 0800 UTC 31, 2000 UTC 30, and 1600 UTC 30 July for the MTG, YX, and XT regions, respectively. It should be noted that the wind field was significantly influenced by Typhoon Khanun (2306) and the remnant vortex originating from Typhoon Doksuri (2305) in the present event. As the typhoon gradually moved northwestward and the vortex weakened, the first region to be affected was Xingtai (XT) in the south, then Yixian (YX) in the center, and finally Mentougou (MTG) in the north, suggesting that the wind shift occurred at a different moment.

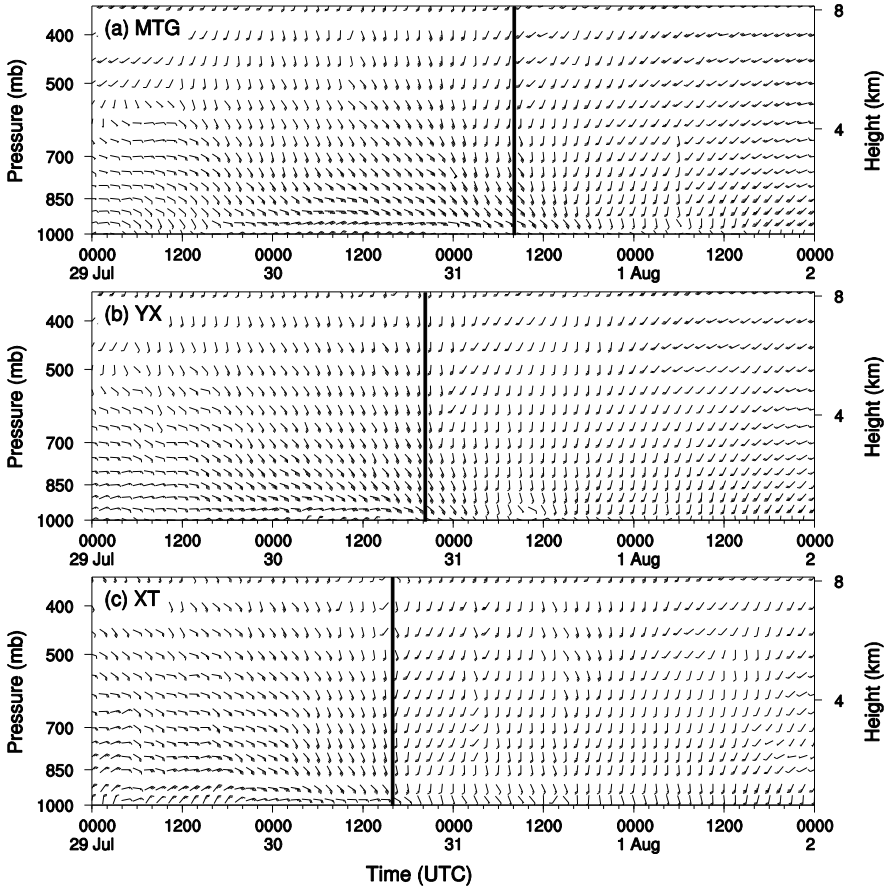

Fig. 8 Same as Fig. 2 but for the simulated. The black lines denote wind shift from southeasterly to southerly/southwesterly over the levels in the low to middle troposphere, which roughly divided the rainfall event into two stages.

4. Unique features for the extreme rainfall

4.1 Dominant dynamic processes for convection initialization

The evolution of dynamical and thermal systems of the rainfall event in the first stage is shown in Fig. 9. Although only a remnant vortex remained over central China at this time, typhoon Doksuri had an important influence on the WNPSH when it was strong as a super

typhoon. Several days before the rainfall event, the super typhoon Doksuri was close to the WNPSH, and the southwest WNPSH edge was within the typhoon's outer region. Owing to the inflow mass flux entering the typhoon region, the southwest part of WNPSH was severely weakened by typhoon Doksuri (Sun et al.,2015). As a result, the west boundary of the WNPSH appeared to an eastward retreat from 500 hPa to 850 hPa, showing an inclined vertical distribution on its western boundary, especially from 700 hPa to 850 hPa. Capped by the inclined WNPSH, water vapor was mainly transported to North China through a passage nearly under 850 hPa that is built by the typhoon remnant vortex combined with the tropical storm Khanun. At 500 hPa (Fig. 9a), the WNPSH (represented by the 588 isoline) covered a large part of eastern China, with an unusual westward extension of the northwest corner to northwestern China. At that time, the northwest corner extended much further westward, compared to that before 12-h (Fig. 3). Similar patterns can be seen at 700 hPa (Fig. 9b), but the west boundary of WNPSH (represented by the 316 isoline) retreated to the East China Sea except for the northwest corner. At 850 hPa (Fig. 9c), the WNPSH (represented by the 156 isoline) completely retreated to the Western North Pacific, far away from China.

The spatial distribution of the high PW was consistent with that of a large equivalent potential temperature (θ_e) of 344K at 500 hPa, indicating that the 334K contour covered a relatively warm and/or wet region (Fig. 9a). Most importantly, the boundary of the high PW corresponded to the large value of the potential temperature gradient over 8K on the east side and 12K on both north and west sides. Previous studies (e.g., Rao et al.,2023) proposed that the heavy rainfall region was closely attributed to the distributions of θ_e. Although the warm and moist conditions were favorable for precipitation, the unfavorable large-scale forcings explain well why no deep convection was formed over this region (marked with a dashed-line box in Fig. 9c, d). The convergence, resulting from changes in wind direction and wind speed, was conducive to triggering convection. Consequently, the weak convergence led to weak lifting and consequent precipitation. Since the convergence occurred at the junction of cold and warm air masses, like a warm front rainfall, rainfalls were formed in low intensity but long duration and widespread coverage. It is important to note that the spatial distribution of rainfall is usually considered to be consistent with the western boundary of WNPSH (i.e., the 588 isoline) at 500 hPa. However, the spatial distribution of rainfall in the present event is consistent with the dense zone of θ_e, instead of the western boundary of WNPSH. Therefore, in addition to the isoline 588

at 500 hPa, the spatial distribution of θ_e needs to be given more attention in future operational forecasts.

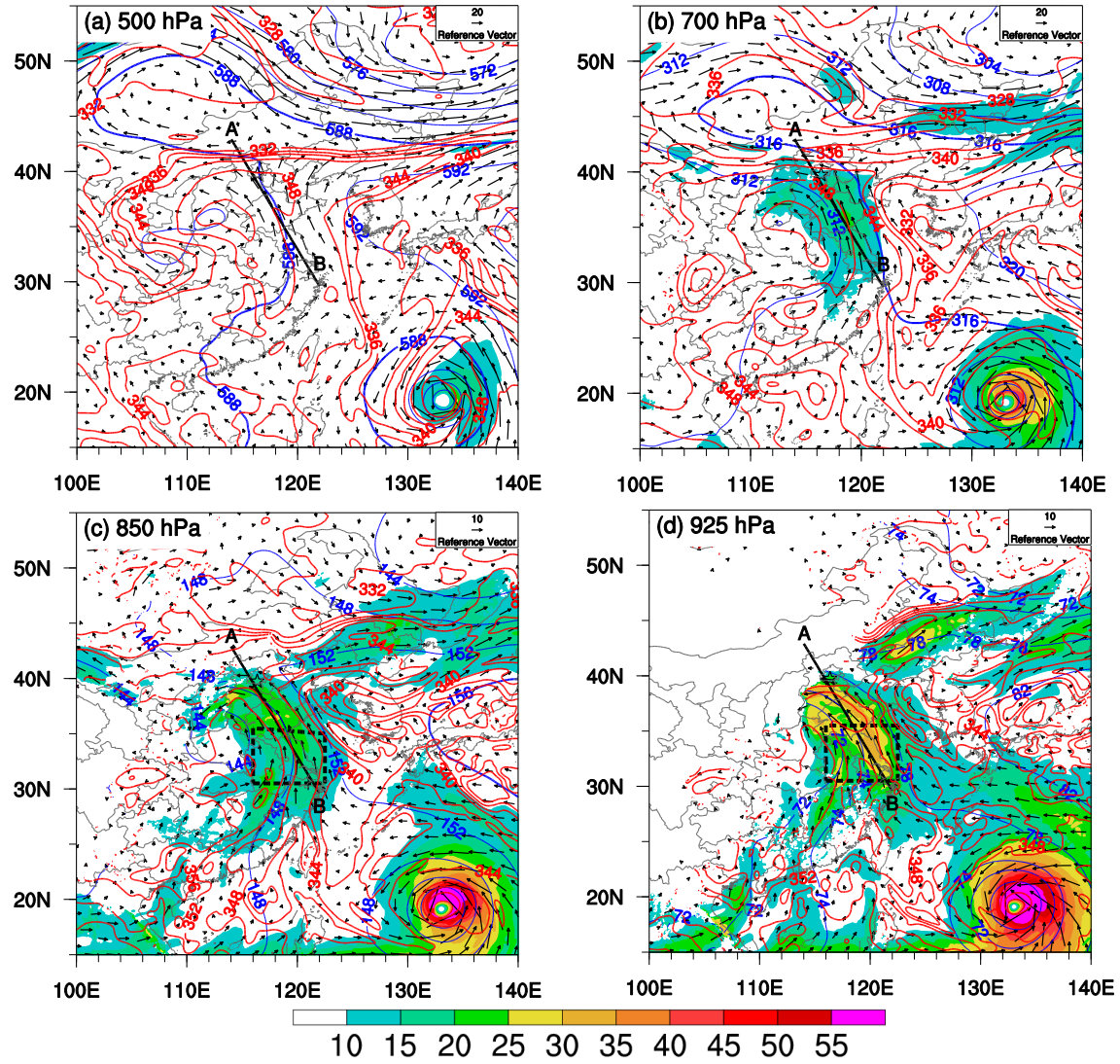

Fig. 9 Spatial distribution of geopotential height (blue contoured at 40 gpm), equivalent potential temperature (red contoured at 2K intervals, θ_e), wind bars (a full barb is 4 m s^{-1}), and water vapor flux (g s^{-1} cm^{-1} hPa^{-1}, shadings) from the model D01 at 0000 UCT 30 July 2023: (a) 500 hPa, (b) 700 hPa, (c) 850 hPa, and (d) 925 hPa. The isolines of 588, 316, and 156 are bolded to represent the WNPSH at 500 hPa, 700 hPa, and 850 hPa, respectively. The convergence zone of southeast and southwest flows is marked by a dashed line box in panels (c) and (d). The thick black line A–B denotes the locations for cross-section along the water vapor transport pathway used in Fig. 10.

The warm and moist features over North China can also be seen from the cross-section along the line A–B as shown in Fig. 10. The western orography region was occupied by cold air mass over the levels above 3.0 km. Under the conditions, significant equivalent potential temperature gradients were established between the warm and cold air masses, similar to a

warm front. Meanwhile, owing to the blocking of orography below 1.3 km and the strong cold air mass above 3.0 km, only the southeasterly flows between 1.3 and 3.0 km above the sea level can overpass the mountains. It should be noted that although the warm and moist southeasterly flows were lifted by the orography, they could not move further upward to trigger convection because of the local capped cold and dry air masses overhead. Consequently, convergence mainly resulted from the changes in wind direction and wind speed caused upward motion. As the warm and moist air was lifted, condensation occurred and even generated precipitation. It should be emphasized that the lifting was too weak to allow convection to be highly organized (Fig. 10). For example, the updrafts in strong deep convective systems (e.g., Yin et al.,2020; Yin et al.,2022c) are 5-10 times as large as the updrafts in the present event. Therefore, the weak lifting was responsible for the rainfall in large coverage but low intensity. Besides, the continuous and stable water vapor supply was another favorable factor for the precipitation.

Also from Fig. 10, one can see that North China was surrounded by warm dry air masses on the east side and cold dry air masses on both north and west sides. More specifically, the air mass at the levels above 1 km on the east side was over 3℃ warmer than surrounding regions, but the water vapor mixing ratio (q_v) was less than 14 g kg^{-1} (humidity was less than 70%) because this region was controlled by the WNPSH. The warm-dry cap overhead explains well the absence of convection and rainfall over this region (cf. Figs. 5 and 6). On the north and west sides, the air masses were dry with q_v less than 2 g kg^{-1}. The air was over 3℃ colder than the surrounding region except for the air near the ground. In view that warm air near the ground might be associated with radiative heating from the ground, owing to being capped by the cold and dry air overhead, it would be understandable why convection could not be enhanced over the mountains.

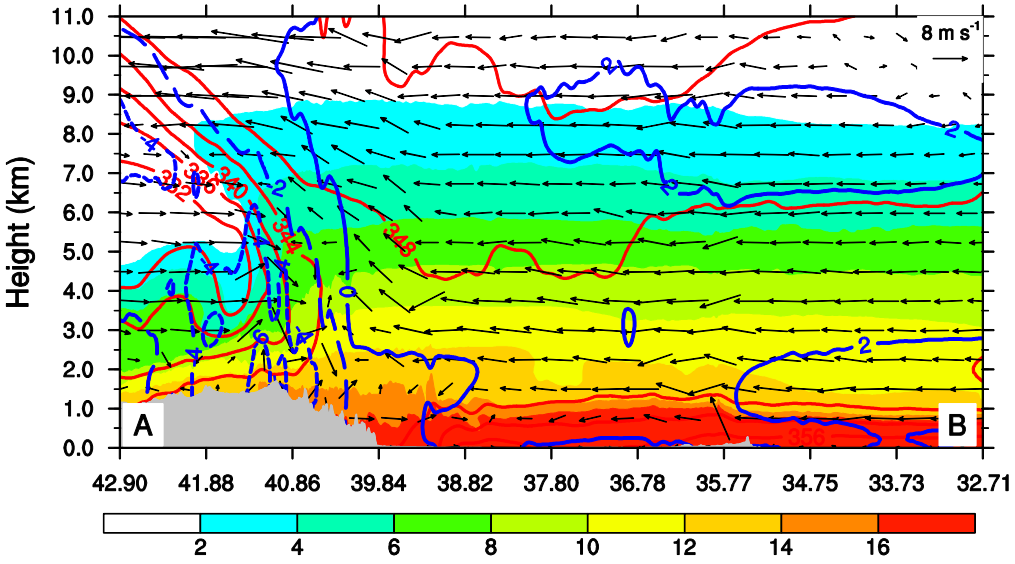

Fig. 10 Vertical cross-section along line A–B given in Fig. 9 of temperature deviations (blue-contoured at 2°C intervals) from their level-averaged values in the cross-section, equivalent potential temperature (red-contoured at 4K intervals), water vapor mixing ratio (q_v, g kg^{-1}, shadings), and in-plane flow vectors (vertical motion amplified by a factor of 20) at 0000 UCT 30 July 2023, respectively. Gray shadings denote terrain.

In the second stage (Fig. 11), obvious differences in dynamical and thermal processes can be seen, compared to those in the first stage (cf. Fig. 9). At 500 hPa (Fig. 11a), the WNPSH further expanded westward with its western border reaching western China. It should be emphasized that the southwestern part of WNPSH was severely damaged by the rapid intensification of Khanun into a super typhoon. Meanwhile, as the trough deepened over northeastern China, cold air from the north poured southward. Consequently, a north-south orientated θ_e dense zone was established over eastern China. Similar patterns in θ_e and horizontal wind field can be seen at 700 hPa (Fig. 11b). However, the WNPSH (represented by the 316 isoline) was further disrupted as the Khanun continued to intensify, appearing that the WNPSH retreated to the East China Sea except for the northwest corner. The north-south orientated θ_e dense zone greatly prevented water vapor from transporting to North China above 850 hPa, and thus water vapor was mainly transported to North China by a shallow southeasterly flow near the ground (Fig. 11c, d). Consequently, the water vapor flux was significantly reduced (Fig. 12a). Besides, North China was dominated by southerly flows over levels above 500 hPa, and thus mid-tropospheric wind shear was significantly enhanced.

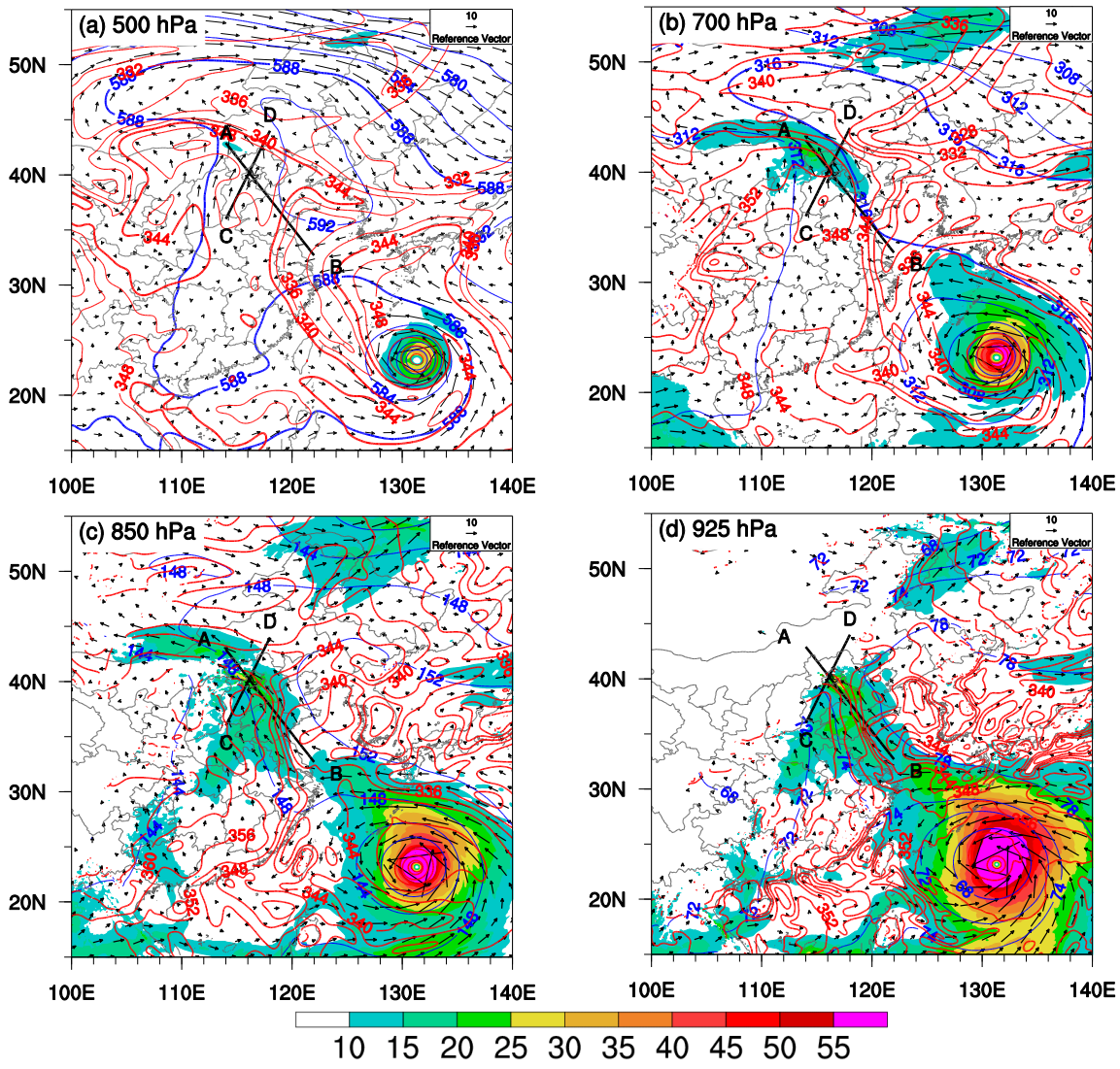

Fig. 11 Same as Fig. 9 but for 0800 UTC 31 July 2023. Thick black lines A–B and C–D denote the locations for the cross-section in Fig. 12.

As addressed above, it was the variation in environmental conditions that caused consequent rainfall changes in nature. Especially, the shift in the wind field brought changes in thermodynamic processes and water vapor sources. Before the wind shift (Figs. 9 and 10), water vapor was mainly from the East China Sea associated with the cyclonic circulation of the typhoon remnant vortex and the tropical storm Khanun and southeasterly flow below 925 hPa. After the shift, water vapor flux was significantly reduced from both southwesterly and southeasterly flows (Fig. 11). Under such a framework, convections were largely triggered by orographic blocking and lifting of southerly/southwesterly flows as convective instability air approached the orography (Fig. 12). Unlike in the first stage, convections were further developed northward over mountains, forming deep convections (Fig. 12b), which might be

attributed to the fact that the cold air on the north side moved northward. Generally speaking, the convections in the second stage are much stronger and deeper than those in the first stage. Consequently, the rainfall intensity is increased, compared to those in the first stage (Figs. 7d,e).

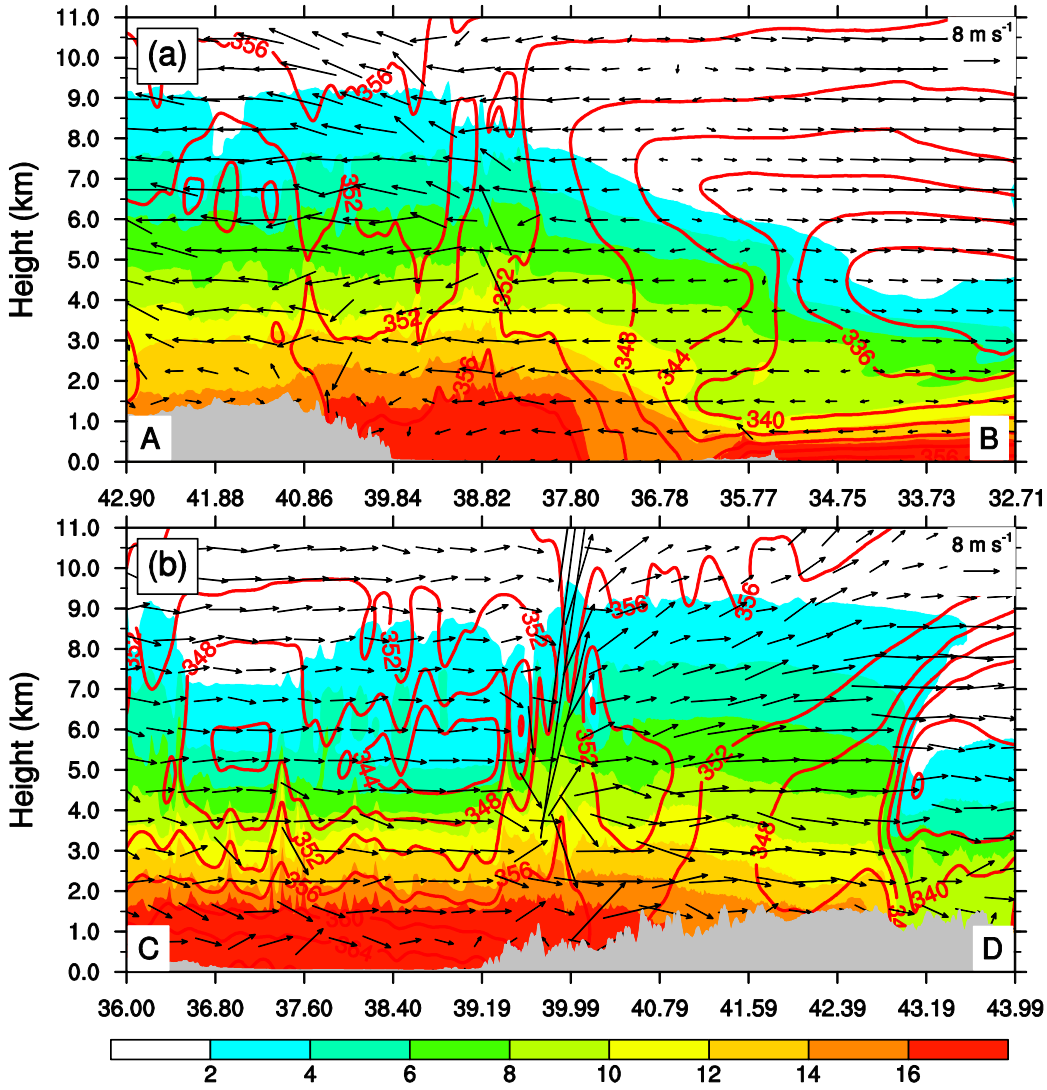

Fig. 12 Vertical cross-sections along lines (a) A–B and (b) C–D given in Fig. 11 of equivalent potential temperature (θ_e, red-contoured at 4K intervals), water vapor mixing ratio (q_v, g kg^{-1}, shadings), and in-plane flow vectors (vertical motion amplified by a factor of 10) at 0800 UCT 31 July 2023. Gray shadings denote terrain.

4.2 Moisture budget

The shift in wind direction and speed implies a change in water vapor source and rainfall properties (Fig. 13). As stated above, water vapor was mainly from the East China Sea associated with the cyclonic circulation of typhoon Khanun before the wind shift, and was

fueled by the southeasterly flow below 925 hPa. After the shift, the water vapor supply was significantly reduced due to both southwesterly and southeasterly flow variations. Figure 13 shows the time-height cross-sections of moisture flux across eastern, southern, western, and northern boundaries and total lateral boundary moisture flux for the MTG region. The moisture flux is calculated by

$$QFlux = \int_0^L q_v \vec{v} dl \, .$$

Here, *QFlux* is moisture flux across one of the four boundaries, and q_v, $\vec{v}$, and L are water vapor mixing ratio, wind vector, and the length of the boundary, respectively. The TOT is a summation of the *QFluxs* from the four boundaries by taking inward (outward) as positive (negative).

One can see that the MTG region experienced vigorous lower-to-middle level inward (outward) moisture fluxes across their eastern and southern (western and northern) boundaries. For the eastern boundary (Fig. 13a), the inward moisture flux began to increase gradually from 0000 UTC 29 July, with the maximum values over 13,500 kg kg^{-1} m^2 s^{-1} occurring between 1200 UTC 30 and 0000 UTC 31 July 2023. Then, the inward flux moisture decreased rapidly and even transformed to the outward flux at 0000 UTC 1 August 2023. The inward moisture flux was mainly concentrated below 3 km above the sea level because upper levels were capped by the warm dry air masses associated with the WNPSH (cf. Figs. 9 and 10) movement. However, owing to weak lifting over, most of the water vapor flowed out through the western boundary (Fig. 13b). Meanwhile, part water vapor was transported in this region from the southern boundary except for the lower levels during 0000 UTC 30 to 0000 UTC 31 July 2023 (Fig. 13d). The outward flow water vapor is caused by the northeasterly branch around flow due to the blocking of the Yanshan Mountains. Similar patterns can be found in the northern boundary with almost the same outward water vapor flux (Fig. 13c). The temporal evolution of the water vapor flux across the eastern boundary is consistent with that of rainfall over this region (Figs. 13a and 7d), suggesting that rainfall formation was dominated by the inward of water vapor from the eastern boundary. Overall, the inward net moisture fluxes were concentrated in the lower troposphere between 0.5 km and 1.5 km (Fig. 13e), suggesting that

most of the water vapor was consumed at this layer by condensation. Despite the high water vapor flux, the water vapor-rich layer is too thin (nearly 1 km) to be favorable for the formation of severe rainfall. Similar patterns can be found over both YX and XT regions (not shown), although there were temporal and quantitative differences.

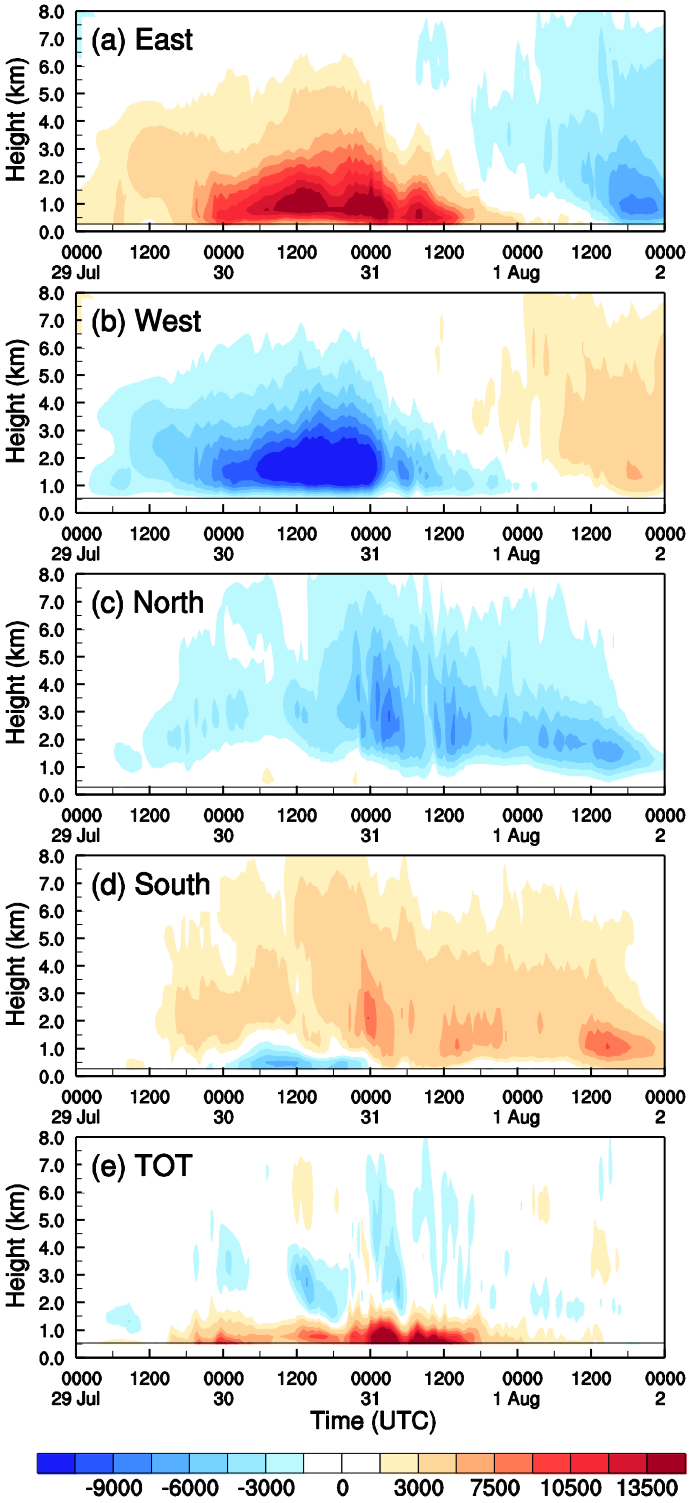

Fig. 13 Time-height cross-sections of the moisture fluxes (kg kg^{-1} m^2 s^{-1}) through the (a) eastern, (b) western, (c) northern, and (d) southern boundaries of the MTG region in Fig. 1; (e)

TOT provides the total net moisture flux of all boundaries.

In the second stage, the north-south orientated θ_e dense zone greatly prevented water vapor from being transported to North China by southeasterly flows from the East China Sea, and thus water vapor was mainly transported to North China across the south boundary (Figs. 13b, d). Unlikely, the water vapor was mainly provided by southeasterly (southwesterly) flow below(above) 500 hPa. Figure 13 shows the time-height cross-sections of the moisture fluxes. It is seen from Fig. 13 that the water vapor flux amount was significantly reduced. Despite the thickening of the water vapor flux layer associated with the southerly/southwesterly flows, the water vapor flux is much less, compared to the first stage. Therefore, the wind shift had strong effects on the reduction in water vapor flux and consequent rainfall over North China. The same results can also be obtained in the YX and XT regions (not shown). It is worth emphasizing that strong hourly rainfalls occurred during the wind shift period (cf. Figs. 2, 7, and 8), suggesting that the changes in wind direction enhanced wind shear and thus promoted the development of convections and consequent precipitation under moisture and instability conditions (Chen et al., 2015; Rotunno et al.,1988; Schumacher and Rasmussen,2020). Therefore, it is important to pay special attention to environmental wind alterations in future remote rainfall forecasts.

4.3 Properties of convection

Figure 14 shows the temporal evolution of maximum upward motion and radar reflectivity over the MTG region during the rainfall period from 0000 UTC 29 to 0000 UTC 2 August 2023. In the first stage (i.e., before 0800 31 July), most of the maximum updrafts were almost less than 3 m s^{-1}. Owing to the weak updrafts, the storm did not stretch as high as typical convective systems over North China, with hydrometeors concentrated on the levels with a temperature above 0℃ (Fig. 14a). As addressed above (Fig. 10), weak updrafts were attributed by the unfavorable large-scale conditions. The vertical distribution of hydrometeor indicates that the warm rain processes were dominant in the persistent rainfall event. The result is consistent with the water vapor consumed layer between 0.5 km and 1.5 km (Fig. 13e). Unlikely, the maximum updraft was over 11 m s^{-1} in the second stage (i.e., after 0800 31 July), which is much stronger than that in the first stage (Fig. 14). Correspondingly, the radar reflectivity penetrated through the 0°C level with a cloud top exceeding 12 km, indicating that both warm and cold rain

processes were active in this stage. Correspondingly, the intensity of hourly rainfall increased significantly, with the maximum value exceeding 100 mm (Fig. 7d). Generally speaking, there are larger strong convective areas in the second than those in the first stage. The same features were also found in the regions of YX and XT (not shown). Unlike the usual short-duration heavy rainfall in North China (Mao et al.,2018; Xia and Zhang,2019; Yin et al.,2022b; Li et al., 2024), this precipitation was mainly dominated by warm cloud processes (Fig. 14), consistent with observations (e.g., Fu et al., 2023). As addressed above, the weak updrafts with warm-moist air were responsible for persistent rainfall but low intensity. A detailed analysis of cloud microphysical processes for this event will be given in a forthcoming study, in which all microphysical source and sink terms will be explained.

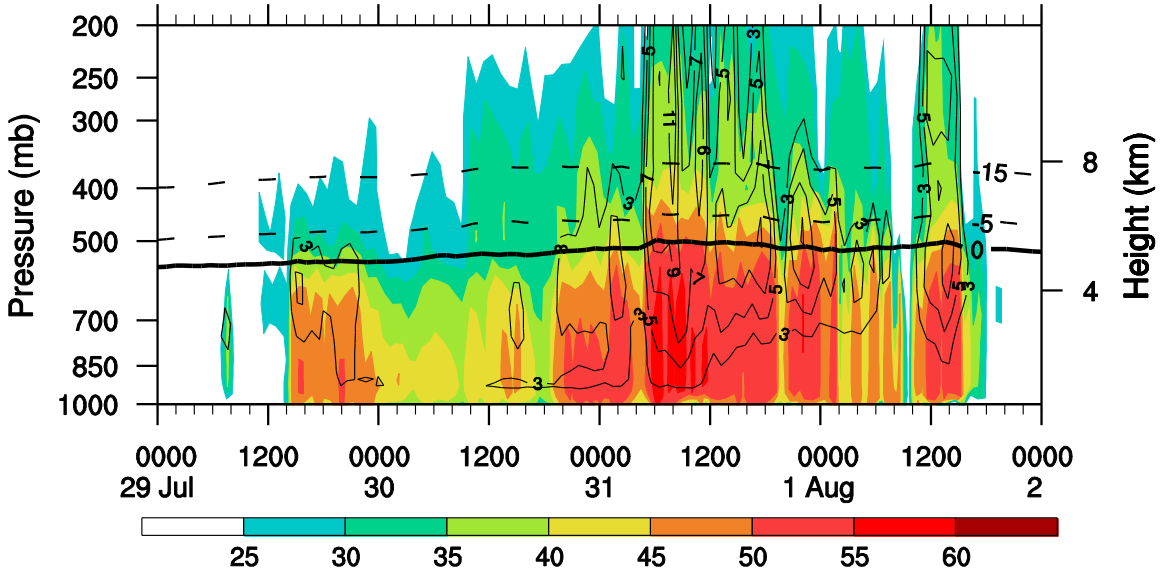

Fig. 14 Time-height cross-section of domain maximum radar reflectivity (dBz, shadings) and upward motion (contoured at 2 m s^{-1}) taken from MTG region during the period from 0000 UTC 29 to 0000 UTC 2 August 2023. The isothermal lines denote the 0°C (the melting layer), -5°C, and -15°C levels, respectively.

5. Conclusions and outlook

In this study, we examined the convective initiation and subsequent persistent heavy rainfall over North China during the period from 29 July to 2 August 2023 in terms of observations and simulations with the WRF model. From observations, the rainfall was featured by long duration and widespread coverage but low intensity, like a warm front rainfall. Firstly, the persistent severe rainfall event was reproduced by the WRF model. Further

477 analysis based on the simulations shows that this persistent precipitation was caused by a
478 combination of a remnant vortex originating from typhoon Doksuri (2305), the tropical storm
479 Khanun (2306), the Western North Pacific subtropical high (WNPSH) with an unusual
480 westward extension of the northwestern corner, and stable cold dry air from over northern
481 China.

482 According to the simulated wind profiles and rainfall features, the persistent heavy rainfall
483 event was divided into two stages. Figure 15 summarizes the synoptic-scale forcings and
484 possible dynamic mechanisms for the persistent heavy rainfall. In the first stage (Fig. 15a), a
485 water vapor transportation passage was built by a typhoon remnant vortex and a tropical storm
486 Khanun, providing a stable warm moist water vapor supply. Several days before the rainfall
487 event, the southwestern WNPSH was within the typhoon Doksuri's outer region, and thus the
488 southwestern WNPSH was weakened by the tropical storm Doksuri. It appears that the west
489 boundary of the western North Pacific subtropical high (WNPSH) retreated eastward from 500
490 hPa to 850 hPa, showing an inclined vertical distribution on the western boundary, especially
491 from 700 hPa to 850 hPa. Capped by the inclined WNPSH, water vapor was mainly transported
492 to North China through a water vapor passage under nearly 850 hPa (Fig. 10). Although the
493 warm and moist regions were favorable for precipitation over North China, organized strong
494 convective systems were seldom because of the absence of favorable large-scale conditions. At
495 the same time, the orography in the western part of North China was occupied by dry cold air
496 mass over levels above 3.0 km. Owing to the blockings of orography below 1.3 km and the
497 strong cold air mass above 3.0 km, only the southeasterly flows between 1.3 and 3.0 km above
498 the sea level can overpass the mountains. Although the warm and moist southeasterly flows
499 were lifted by the orography, they could not go further upward to trigger convections because of
500 the locally capped cold and dry air masses overhead. Under the conditions, significant
501 equivalent potential temperature gradients were established between the warm and cold air
502 masses, similar to a warm front. Consequently, convergence mainly resulted from the changes
503 in wind direction and wind speed led to upward motion. As the warm and moist air was lifted,
504 condensation occurred and further generated precipitation. However, the lifting was too weak
505 to allow convection to be highly organized (Fig. 14), leading to the rainfall in low intensity but

large coverage. Besides, the continuous and stable transportation of water vapor provided by tropical storm Khanun ensured stable precipitation over a long period of over 80 h. Therefore, this event shows similar rainfall features to those of a warm front rainfall with a long duration and widespread coverage but low intensity.

In the second stage (Fig. 15b), the WNPSH further expanded westward at 500 hPa, with its western border reaching western China. However, the southwest part of WNPSH was further damaged by the rapid intensification of Khanun into a super typhoon. Consequently, the embedded warm-dry cover associated with the tilted WNPSH was significantly thinned, favoring convective development. Meanwhile, as the trough deepened over northeastern China, cold air from the north poured southward. Consequently, a north-south-orientated equivalent potential temperature (θ_e) dense zone was established over eastern China, which greatly prevented water vapor from being transported to North China (Fig. 12a). However, owing to the clockwise rotated southeasterly flow, a deep southerly /southwesterly flow was built over North China. The convections were triggered by orographic blocking and lifting of southerly/southwesterly flows as convective instability air approached orography. Unlike the first stage, the convections were further developed northward over mountains, forming deep convections. It should be noted that the northward-moved cold air on the north side was another favorable condition. Therefore, the convections in the second stage are much stronger and deeper than those in the first stage, although water vapor flux is smaller in the second period. Consequently, the rainfall intensity is increased, compared to that in the first stage. Correspondingly, both warm and cold rain processes were active in the second stage, while warm rain processes were dominant in the first stage.

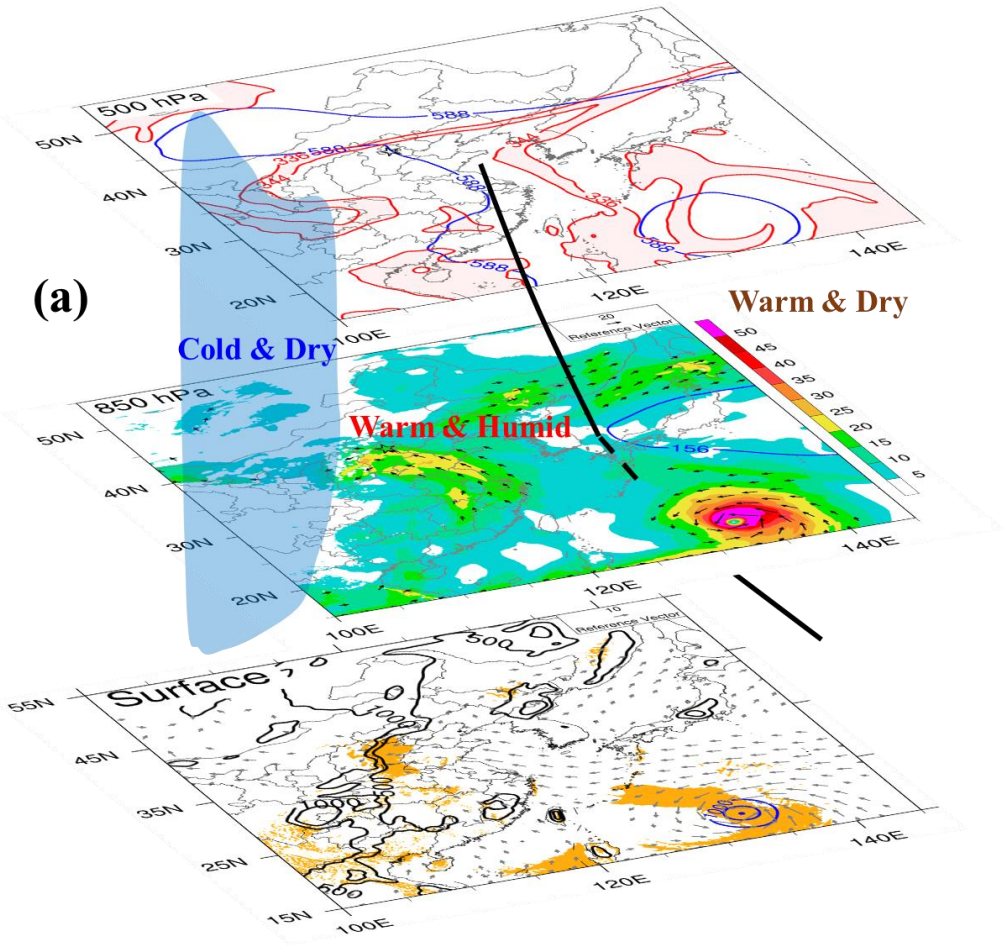
(a)
500 hPa
588
336
344
Cold & Dry
Warm & Dry
850 hPa
Warm & Humid
158
Surface
1000
50N
40N
30N
20N
55N
45N
35N
25N
15N
100E
120E
140E

528

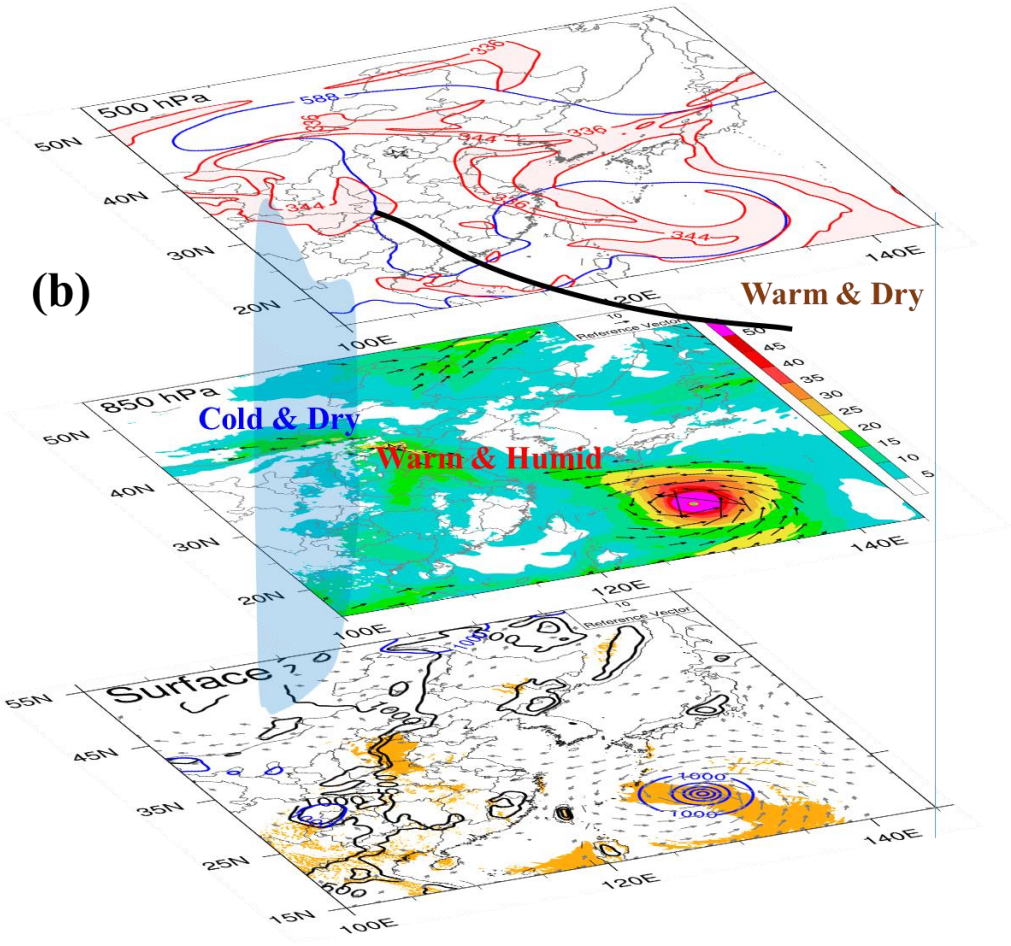
(b)
500 hPa
588
336
344
Warm & Dry
850 hPa
Cold & Dry
Warm & Humid
Surface
1000
50N
40N
30N
20N
55N
45N
35N
25N
15N
100E
120E
140E

529

Fig. 15 (a) Three-dimensional diagram of the mechanisms for the persistent heavy precipitation in the first stage. Several distinct synoptic systems, including the tropical storm Khanun (2306), a remnant vortex originating from the typhoon Doksuri (2305), quasi-stationary cold dry air masses, and an abnormal Western North Pacific subtropical high (WNPSH) with inclined vertical distribution on the western boundary (thick black line). Blue lines marked with 588 and 156 represent the WNPSH at 500 hPa and 850 hPa, respectively. Red lines denote the spatial distribution of equivalent potential temperature (θ_e) dense zone between 336 K and 344K. At 850 hPa, black arrows indicate jets with wind speed over 12 m s^{-1}, and shadings denote water vapor flux. Orange shadings imply 96-h accumulated rainfall over 200 mm; blue contours denote sea level pressure; gray arrows denote surface (i.e., z =10 m) horizontal wind with wind speed over 5 m s^{-1}, and black contours indicate orography (m). (b) Same as (a) but for rainfall in the second stage.

In this study, we have gained principal results of the persistent heavy rainfall event. It is important to note that the spatial distribution of rainfall is usually considered to be consistent with the western boundary of WNPSH (i.e., the 588 isoline) at 500 hPa. In the present event, the spatial distribution of rainfall is consistent with the dense zone of θ_e, rather than the western boundary of WNPSH. Therefore, in addition to the 588 isoline, the spatial distribution of θ_e needs to be given more attention in future operational forecasts. Besides, we should give weight to environmental wind shifts, which may lead to changes in convections and the nature of consequent precipitation. Although reasonable dynamic mechanisms for the present persistent heavy rainfall have been proposed, there are still several questions that need to be answered. Among those, more work is required to understand detailed cloud and precipitation processes. In addition, diagnostic and budget analyses will be conducted to understand how the orography facilitates the generation of the rainfall belt with three rainfall cores along the mountains. Nevertheless, the concept of synoptic-forcing-based forecasting is discussed as it might apply to a broader spectrum of forecast events than just over North China.

Code and data availability

The source code of the Weather Research and Forecasting model (WRF v4.1.3) is available at https://github.com/wrf-model/WRF/releases (last access 1 August 2024). The National

Centers for Environmental Prediction (NCEP) Global Forecast System one-degree final analysis data at 6 h intervals used for the initial and boundary conditions for the specific analyzed period can be downloaded at https://rda.ucar.edu/datasets/d083002/ (last access 1 August 2024). Modified WRF model codes and all the data used in this study are available from the authors upon request.

Author contributions

Conceptualization: JY, JS, and XL; methodology: JY and JS; data curation: JY and FL; writing – original draft preparation: JY, and FL; writing – review and editing: JY, ML, RX, XB, and JS; project administration: XL; funding acquisition: JY and XL. All authors have read and agreed to the published version of the paper.

Competing interests

The contact author has declared that none of the authors has any competing interests.

Acknowledgments

The authors acknowledge the use of the NCAR Command Language (NCL) in the preparation of figures.

Financial support

This study is jointly supported by the National Key R&D Program of China (2022YFC3003903), National Natural Science Foundation of China (42075083), Open Project Fund of China Meteorological Administration Basin Heavy Rainfall Key Laboratory (2023BHR-Z03), Basic Research Fund of Chinese Academy of Meteorological Sciences (2023Z001), and the Development Foundation of Chinese Academy of Meteorological Sciences (2019KJ026).

References

Bao, X., Sun, J., Yin, J., Gao, X., Li, F., Liang, X., Gu, H., Xia, R., Li, M., Wu, C., and Feng, J.: What Caused the Differences between “23·7” and “96·8” Extreme Rainfall Events in North China under a Similar Synoptic Background?, Journal of Meteorological Research, 38, 861-879, https://doi.org/10.1007/s13351-024-3192-0, 2024.

Bowden, J. H., Otte, T. L., Nolte, C. G., and Otte, M. J.: Examining Interior Grid Nudging Techniques Using Two-Way Nesting in the WRF Model for Regional Climate Modeling, J. Clim., 25, 2805-2823, https://doi.org/10.1175/JCLI-D-11-00167.1, 2012.

Chen, Q., Fan, J., Hagos, S., Gustafson Jr, W. I., and Berg, L. K.: Roles of wind shear at different vertical levels: Cloud system organization and properties, Journal of Geophysical Research: Atmospheres, 120, 6551-6574, https://doi.org/10.1002/2015JD023253, 2015.

Ding, Y.: A case study on the excessively severe rainstrom in Honan province, early in August, 1975, Scientia Atmospherica Sinica, 2, 276-289. (in Chinese), 1978.

Dudhia, J.: Numerical Study of Convection Observed during the Winter Monsoon Experiment Using a Mesoscale Two-Dimensional Model, Journal of the Atmospheric Sciences, 46, 3077-3107, https://doi.org/10.1175/1520-0469(1989)046<3077:NSOCOD>2.0.CO;2, 1989.

Feng, W. and Cheng, L.: Nonhydrostatic numerical simulation for the "96.8" extraordinary rainstorm and the developing structure of mesoscale system, 16, 423-440, 2002.

Fowler, H. J., Blenkinsop, S., Green, A., and Davies, P. A.: Precipitation extremes in 2023, Nature Reviews Earth & Environment, 5, 250-252, https://doi.org/10.1038/s43017-024-00547-9, 2024.

Fu, J., Quan, W., Mai, Z., Luo, Q., Chen, T., Li, X., Xu, X., Zhu, W., Hua, S., and Han, X.: Preliminary study on the refined characteristics of rainfall intensity and dynamic and thermodynamic conditions in the July 2023 severe torrential rain in north China, Meteorological Monthly, 49, 1435-1450, 10.7519/j.issn.1000-0526.2023.112701, 2023. (In Chinese with English abstract)

Gao, Z., Zhang, J., Yu, M., Liu, Z., Yin, R., Zhou, S., Zong, L., Ning, G., Xu, X., Guo, Y., Wei,

H., and Yang, Y.: Role of Water Vapor Modulation From Multiple Pathways in the Occurrence of a Record-Breaking Heavy Rainfall Event in China in 2021, Earth and Space Science, 9, e2022EA002357, https://doi.org/10.1029/2022EA002357, 2022.

Gao, X., Sun, J., Yin, J., Abulikemu, A., Wu, C., Liang, X., and Xia, R.: The impact of mountain-plain thermal contrast on precipitation distributions during the "23·7" record-breaking heavy rainfall over North China, Atmospheric Research, 107582, https://doi.org/10.1016/j.atmosres.2024.107582, 2024.

Hirata, H. and Kawamura, R.: Scale interaction between typhoons and the North Pacific subtropical high and associated remote effects during the Baiu/Meiyu season, Journal of Geophysical Research: Atmospheres, 119, 5157-5170, https://doi.org/10.1002/2013JD021430, 2014.

Hong, S.-Y., Dudhia, J., and Chen, S.-H.: A Revised Approach to Ice Microphysical Processes for the Bulk Parameterization of Clouds and Precipitation, Monthly Weather Review, 132, 103-120, https://doi.org/10.1175/1520-0493(2004)132<0103:ARATIM>2.0.CO;2, 2004.

Hu, G., Lu, M.-H., Reynolds, D., Wang, H.-K., Chen, X., Liu, W.-C., Zhu, F., Wu, X.-W., Xia, F., Xie, M.-C., Cheng, X.-N., Lim, K.-S., Zhai, B.-P., and Chapman, J.: Long-term seasonal forecasting of a major migrant insect pest: the brown planthopper in the Lower Yangtze River Valley, J. Pest Sci., 92, https://doi.org/10.1007/s10340-018-1022-9, 2019.

Janjić, Z. I.: The step-mountain eta coordinate model: further developments of the convection, viscous sublayer, and turbulence closure schemes, Monthly Weather Review, 122, 927-945, https://doi.org/10.1175/1520-0493(1994)122<0927:TSMECM>2.0.CO;2, 1994.

Janjić, Z. I.: Nonsingular implementation of the Mellor-Yamada Level 2.5 Scheme in the NCEP Meso model. NCEP Office Note No. 437, 61 pp., 2002.

Jiménez, P. A., Dudhia, J., González-Rouco, J. F., Navarro, J., Montávez, J. P., and García-Bustamante, E.: A Revised Scheme for the WRF Surface Layer Formulation, Monthly Weather Review, 140, 898-918, https://doi.org/10.1175/MWR-D-11-00056.1, 2012.

643 Kain, J. S.: The Kain–Fritsch Convective Parameterization: An Update, Journal of Applied
644 Meteorology, 43, 170-181,
645 https://doi.org/10.1175/1520-0450(2004)043<0170:TKCPAU>2.0.CO;2, 2004.
646 Li, H., Yin, J., and Kumjian, M.: ZDR Backwards Arc: Evidence of Multi-Directional Size
647 Sorting in the Storm Producing 201.9 mm Hourly Rainfall, Geophys. Res. Lett., 51,
648 e2024GL109192, https://doi.org/10.1029/2024GL109192, 2024.
649 Li, M., Sun, J., Li, F., Wu, C., Xia, R., Bao, X., Yin, J., and Liang, X.: Precipitation Evolution
650 from Plain to Mountains during the July 2023 Extreme Heavy Rainfall Event in North
651 China, Journal of Meteorological Research, 38, 635-651, 10.1007/s13351-024-3182-2,
652 2024.
653 Lin, Y.-H. and Wu, C.-C.: Remote Rainfall of Typhoon Khanun (2017): Monsoon Mode and
654 Topographic Mode, Monthly Weather Review, 149, 733-752,
655 https://doi.org/10.1175/MWR-D-20-0037.1, 2021.
656 Mao, J., Ping, F., Yin, L., and Qiu, X.: A Study of Cloud Microphysical Processes Associated
657 With Torrential Rainfall Event Over Beijing, Journal of Geophysical Research:
658 Atmospheres, 123, 8768-8791, https://doi.org/10.1029/2018JD028490, 2018.
659 Meng, Z., Zhang, F., Luo, D., Tan, Z., Fang, J., Sun, J., Shen, X., Zhang, Y., Wang, S., Han, W.,
660 Zhao, K., Zhu, L., Hu, Y., Xue, H., Ma, Y., Zhang, L., Nie, J., Zhou, R., Li, S., Liu, H., and
661 Zhu, Y.: Review of Chinese atmospheric science research over the past 70 years: Synoptic
662 meteorology, Science China Earth Sciences, 62, 1946-1991,
663 https://doi.org/10.1007/s11430-019-9534-6, 2019.
664 Mlawer, E. J., Taubman, S. J., Brown, P. D., Iacono, M. J., and Clough, S. A.: Radiative transfer
665 for inhomogeneous atmospheres: RRTM, a validated correlated-k model for the longwave,
666 Journal of Geophysical Research: Atmospheres, 102, 16663-16682,
667 https://doi.org/10.1029/97JD00237, 1997.
668 Tomas, P., Pieter, G., and Ivan, T.: Vertical wind shear and convective storms,
669 https://doi.org/10.21957/z0b3t5mrv, 2021.
670 Rao, C., Chen, G., and Ran, L.: Effects of Typhoon In-Fa (2021) and the Western Pacific

671 Subtropical High on an Extreme Heavy Rainfall Event in Central China, Journal of
672 Geophysical Research: Atmospheres, 128, e2022JD037924,
673 https://doi.org/10.1029/2022JD037924, 2023.
674 Rotunno, R., Klemp, J., and Weisman, M.: A Theory for Strong, Long-Lived Squall Lines,
675 Journal of The Atmospheric Sciences - J ATMOS SCI, 45, 463-485,
676 https://doi.org/10.1175/1520-0469(1988)045<0463:ATFSLL>2.0.CO;2, 1988.
677 Schumacher, R. S. and Rasmussen, K. L.: The formation, character and changing nature of
678 mesoscale convective systems, Nature Reviews Earth & Environment, 1, 300-314,
679 10.1038/s43017-020-0057-7, 2020.
680 Stauffer, D. R., Seaman, N. L., and Binkowski, F. S.: Use of Four-Dimensional Data
681 Assimilation in a Limited-Area Mesoscale Model Part II: Effects of Data Assimilation
682 within the Planetary Boundary Layer, Monthly Weather Review, 119, 734-754,
683 https://doi.org/10.1175/1520-0493(1991)119<0734:UOFDDA>2.0.CO;2, 1991.
684 Sun, J., Qi, L., and Zhao, S.: A study on mesoscale convective systems of the severe heavy
685 rainfall in north China by “9608” typhoon, Acta Meteorologica Sinica, 64, 57-71,
686 10.11676/qxxb2006.006, 2006.
687 Sun, Y., Zhong, Z., Yi, L., Li, T., Chen, M., Wan, H., Wang, Y., and Zhong, K.: Dependence of
688 the relationship between the tropical cyclone track and western Pacific subtropical high
689 intensity on initial storm size: A numerical investigation, Journal of Geophysical Research:
690 Atmospheres, 120, 11,451-411,467, https://doi.org/10.1002/2015JD023716, 2015.
691 Tewari, M., Chen, F., Wang, W., Dudhia, J., LeMone, M. A., Mitchell, K., Ek, M., Gayno, G.,
692 Wegiel, J., and Cuenca, R. H.: Implementation and verification of the unified NOAH land
693 surface model in the WRF model. 20th conference on weather analysis and
694 forecasting/16th conference on numerical weather prediction, pp. 11-15., 2004.
695 Thompson, G., Field, P. R., Rasmussen, R. M., and Hall, W. D.: Explicit Forecasts of Winter
696 Precipitation Using an Improved Bulk Microphysics Scheme. Part II: Implementation of a
697 New Snow Parameterization, Monthly Weather Review, 136, 5095-5115,
698 https://doi.org/10.1175/2008MWR2387.1, 2008.

699 Wang, Y., Wang, Y., and Fudeyasu, H.: The Role of Typhoon Songda (2004) in Producing
700 Distantly Located Heavy Rainfall in Japan, Monthly Weather Review, 137, 3699-3716,
701 https://doi.org/10.1175/2009MWR2933.1, 2009.
702 Xia, R., Ruan, Y., Sun, J., Liang, X., Li, F., Wu, C., Li, J., Yin, J., Bao, X., Li, M., and Gao, X.:
703 Distinct Mechanisms Governing Two Types of Extreme Hourly Rainfall Rates in the
704 Mountain Foothills of North China During the Passage of a Typhoon Remnant Vortex
705 from July 30 to August 1, 2023, Advances in Atmospheric Sciences,
706 https://doi.org/10.1007/s00376-024-4064-3, 2025.
707 Xia, R. and Zhang, D.-L.: An Observational Analysis of Three Extreme Rainfall Episodes of
708 19–20 July 2016 along the Taihang Mountains in North China, Monthly Weather Review,
709 147, 4199-4220, https://doi.org/10.1175/MWR-D-18-0402.1, 2019.
710 Xu, H. and Li, X.: Torrential rainfall processes associated with a landfall of Typhoon Fitow
711 (2013): A three-dimensional WRF modeling study, Journal of Geophysical Research:
712 Atmospheres, 122, 6004-6024, https://doi.org/10.1002/2016JD026395, 2017.
713 Xu, H., Zhang, D., and Li, X.: The Impacts of Microphysics and Terminal Velocities of
714 Graupel/Hail on the Rainfall of Typhoon Fitow (2013) as Seen From the WRF Model
715 Simulations With Several Microphysics Schemes, Journal of Geophysical Research:
716 Atmospheres, 126, e2020JD033940, https://doi.org/10.1029/2020JD033940, 2021.
717 Xu, H., Li, X., Yin, J., and Zhang, D.: Predecessor Rain Events in the Yangtze River Delta
718 Region Associated with South China Sea and Northwest Pacific Ocean (SCS-WNPO)
719 Tropical Cyclones, Advances in Atmospheric Sciences, 40, 1021-1042,
720 https://doi.org/10.1007/s00376-022-2069-3, 2023a.
721 Xu, H., Zhao, D., Yin, J., Duan, Y., Gao, W., Li, Y., and Zhou, L.: Indirect Effects of Binary
722 Typhoons on an Extreme Rainfall Event in Henan Province, China From 19 to 21 July
723 2021. 3. Sensitivities to Microphysics Schemes, Journal of Geophysical Research:
724 Atmospheres, 128, e2022JD037936, https://doi.org/10.1029/2022JD037936, 2023b.
725 Yang, L., Liu, M., Smith, J. A., and Tian, F.: Typhoon Nina and the August 1975 Flood over
726 Central China, Journal of Hydrometeorology, 18, 451-472,

https://doi.org/10.1175/JHM-D-16-0152.1, 2017.

Yin, J., Liang, X., Wang, H., and Xue, H.: Representation of the autoconversion from cloud to rain using a weighted ensemble approach: a case study using WRF v4.1.3, Geosci. Model Dev., 15, 771-786, https://doi.org/10.5194/gmd-15-771-2022, 2022a.

Yin, J., Zhang, D.-L., Luo, Y., and Ma, R.: On the Extreme Rainfall Event of 7 May 2017 Over the Coastal City of Guangzhou. Part I: Impacts of Urbanization and Orography, Monthly Weather Review, 148, 955-979, https://doi.org/10.1175/MWR-D-19-0212.1, 2020.

Yin, J., Gu, H., Yu, M., Bao, X., Xie, Y., and Liang, X.: Synergetic Roles of Dynamic and Cloud Microphysical Processes in Extreme Short-Term Rainfall: A Case Study, Quarterly Journal of the Royal Meteorological Society, 148, 3660- 3676, https://doi.org/10.1002/qj.4380, 2022b.

Yin, J., Wang, D., Liang, Z., Liu, C., Zhai, G., and Wang, H.: Numerical Study of the Role of Microphysical Latent Heating and Surface Heat Fluxes in a Severe Precipitation Event in the Warm Sector over Southern China, Asia-Pacific Journal of Atmospheric Sciences, 54, 77-90, https://doi.org/10.1007/s13143-017-0061-0, 2018.

Yin, J., Gu, H., Liang, X., Yu, M., Sun, J., Xie, Y., Li, F., and Wu, C.: A Possible Dynamic Mechanism for Rapid Production of the Extreme Hourly Rainfall in Zhengzhou City on 20 July 2021, Journal of Meteorological Research, 36, 6-25, https://doi.org/10.1007/s13351-022-1166-7, 2022c.